Thermal Evolution and Radiative Output of Solar Flares Observed by the EUV Variability Experiment (EVE)

P. C. Chamberlin[1] · R. O. Milligan[1] · T. N. Woods[2]

Abstract

This paper describes the methods used to obtain the thermal evolution and radiative output during solar flares as observed by the Extreme ultraviolet Variability Experiment (EVE) onboard the *Solar Dynamics Observatory* (SDO). Presented and discussed in detail are how EVE measurements, due to its temporal cadence, spectral resolution and spectral range, can be used to determine how the thermal plasma radiates at various temperatures throughout the impulsive and gradual phase of flares. EVE can very accurately determine the radiative output of flares due to pre- and in-flight calibrations. Events are presented that show the total radiated output of flares depends more on the flare duration than the typical GOES X-ray peak magnitude classification. With SDO observing every flare throughout its entire duration and over a large temperature range, new insights into flare heating and cooling as well as the radiative energy release in EUV wavelengths support existing research into understanding the evolution of solar flares.

Keywords: Solar Flares, EUV, SDO, Sun, Space Weather

1. Introduction

The *Solar Dynamics Observatory* (SDO) is the first satellite in NASAs Living With a Star (LWS) program which was launched in order to investigate how the Sun drives space weather and physically influences the Earth and other planets (Pesnell, Thompson, and Chamberlin, 2012). The Extreme-ultraviolet Variability Experiment (EVE; Woods *et al.*, 2012), one of the three SDO instruments, was designed to make the connection between how variations in the absolute

[1] Solar Physics Laboratory, Heliophysics Division, NASA
Goddard Space Flight Center, Greenbelt, MD 20771 email:
phillip.c.chamberlin@nasa.gov email: r.milligan@qub.ac.uk
[2] Laboratory for Atmospheric and Space Physics, University
of Colorado, Boulder, CO 80303 email:
tom.woods@lasp.colorado.edu

radiative output at X-ray (0.1-10 nm) and extreme ultraviolet (EUV; 10–106 nm) wavelengths drive physical changes in the Earths upper atmosphere over a wide range of timescales from seconds to minutes during solar flares, from days to weeks during the emergence and disappearance of active regions, and from years to decades over the course of a solar cycle.

Fluctuations in the level of EUV irradiance received at 1 AU are known to drive immediate changes in the ionospheric density leading to sudden frequency deviations (SFDs), particularly during solar flares (Kane and Donnelly, 1971; Donnelly and Kane, 1978). Solar flares have also been shown to drive changes in the neutral density of both the day-side (Sutton *et al.*, 2006) and night-side (Pawlowski and Ridley, 2008) of Earth's thermosphere. Although the flare magnitude is important, Qian *et al.* (2010) recently showed that the atmospheric response is also dependent on the flare's location on the solar disk. The center-to-limb characterization of solar flares will be much improved with EVE observations of multiple flares at various locations on the solar disk. Similar ionospheric effects have also been noted on the ionosphere of Mars (Mendillo *et al.*, 2006; Withers, 2009) as well as determined as a ionizing source of the lunar dust (Sternovsky *et al.*, 2008). All of the above papers demonstrate the need for accurate measurements of the solar EUV irradiance on flare timescales as the effects of changes in the solar output can be seen throughout the solar system.

Although accurately measuring the solar EUV irradiance is important for understanding fluctuations in Earth's ionosphere and thermosphere, studying the Sun's EUV output can be useful for investigating important characteristics of solar flares themselves. The spectral range covered by EVE allows emission over a broad range of temperatures throughout all layers of the solar atmosphere to be observed simultaneously. The temperature of measured emission ranges from chromospheric lines formed at around 80 000 K, through the quiescent corona at a few MK, up to highly ionized emission lines with formation temperatures in excess of 10 MK, found only in flaring plasma. Also included in this range are various radiative recombination continua, such as the Lyman continuum of hydrogen that peaks around 91 nm and dominates the spectra down to almost 60 nm (see Milligan *et al.* 2012). Hudson *et al.* (2011) have also been able to derive Doppler velocities from EVE flare spectra despite its 0.1 nm spectral resolution that has been previously thought to be too coarse to quantify these shifts.

In order to cover such a wide spectral range, EVE comprises three different channels (MEGS-A1, MEGS-A2, and MEGS-B), each with different optical properties which are used to optimize the signal in each range. A sample EVE spectrum is shown in Figure 1, as measured on 3 May 2010 from an EVE proto-type rocket flight. This more complete spectrum is shown in liu of a SDO/EVE spectrum as the final calibration and the data are not yet released for MEGS-B data above 75 nm. The MEGS-A channels, covering 6.5–37 nm, record a complete spectrum every 10 seconds with an almost 100% duty cycle. This complete temporal coverage ensures that all flares are observed, although only those larger than high B-class have significant enough enhancements to be detected above the EVE background level in most wavelengths. The MEGS-B channel, which measures the solar irradiance from 37–106 nm, operates for 3 h per day,

followed by 5 min every hour to track variations throughout the day, and is therefore not optimized for flares due to this reduced duty cycle. EVE also includes EUV Spectro-Photometers (ESP) that measure the solar X-ray and EUV in broad (5–7 nm) channels (Didkovsky *et al.*, 2009) to coincide with four of SDO's Atmospheric Imaging Assembly (AIA; Lemen *et al.*, 2012) wavelength bands. The ESP 0.1–7.0 nm band has been shown to scale with the GOES/XRS 0.1–0.8 nm channel (Woods *et al.*, 2005), and which will be used to accurately quantify the radiative output of the soft X-ray emission in this study.
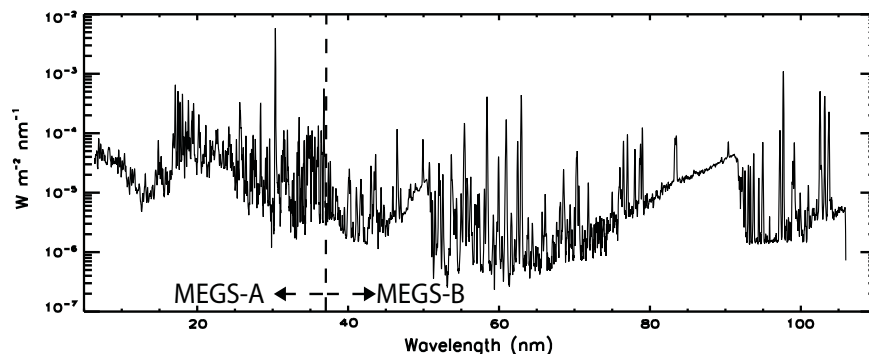

Figure 1. EVE solar spectrum from a rocket calibration flight on 3 May 2010. The wavelength ranges covered by MEGS-A and MEGS-B are noted.

Studying the timing and absolute radiative output of EUV emission formed at different temperatures can help to quantify the energy radiated by different layers of the solar atmosphere throughout a flare. This paper demonstrates EVE's ability to determine the magnitude and timing of isothermal lightcurves during flares as well as the energy radiated at XUV and EUV wavelengths (0.1–37 nm). This will lead to a more accurate understanding of the radiative energy budget and energy transport processes in all phases of the flare, including the late-phase emission that has recently been observed and quantified by Woods *et al.* (2011). Four flares of similar magnitude, but with inherently different characteristics, are described in detail in Section 2 and discussed in terms of their thermal evolution, while Section 3 describes how the thermal evolution can be used to determine the flares' cooling rates. Section 4 describes how the radiative output of these, and several other flares observed in the EUV compare to the corresponding energetics derived from soft X-ray observations taken using the GOES series of satellites. Sections 5 and 6 provide a discussion and conclusion, respectively.

2. Thermal Evolution Plot Formation: M1.2 Flare - 5 May 2010

EVE simultaneously observes emission over a broad range of temperatures, from the upper chromosphere to the hot flaring corona every 10 seconds. In order to visualize the behavior of plasma at different temperatures during solar flares, a thermal evolution plot, which an example can be seen in Figure 2, can be used to show the absolute radiated power at discrete temperatures. This is a

very powerful tool for visualizing the thermal evolution of the flaring plasma, particularly when used in conjunction with other instruments, such as AIA, RHESSI, and the EIS instrument onboard Hinode. The section describes how such plots are constructed.

The first step in constructing a thermal evolution plot is to determine which emissions are isothermal and unblended within the EVE/MEGS spectral range. Each bound-bound emission line is assigned a characteristic formation temperature, T_{max}, based on the peak of the associated contribution function, $G(T)$, from the CHIANTI atomic database (v6.0.1; Dere *et al.*, 1997, 2009). Figure 3 shows two such examples; the Fe XVIII line at 9.39 nm (left panel), and Fe XXII at 13.58 nm (right panel). Both panels in Figure 3 show the measured EVE flare spectrum (minus the pre-flare irradiance spectrum), and also the synthetic CHIANTI spectrum assuming a flare DEM and an electron density of 10^{11} cm^{-3}. It is also apparent that EVE's spectral resolution is approximately 0.1 nm wide, which is denoted by the vertical dashed black lines bounding this range. Examples of the contribution functions corresponding to the two lines shown are shown in Figure 4. The complete, summed contribution function for all emissions within the 0.1 nm spectral range are shown as the dashed black line. For the 9.4 nm line, the dominant emission line is Fe XVIII 9.39 nm formed at $\log(T){=}6.85$, which is plotted as the solid black line, while contributions from other ions are plotted and labeled along with their percentage of the $G(T)$. The 13.58 nm line (right-hand panel) is dominated by the Fe XXII emission at 13.58 nm that has a peak formation temperature of $\log(T){=}7.1$.

To determine whether a given EVE emission line can be considered isothermal, a "quality factor" (QF) is specified. This quality factor is the allowed percentage of the total contribution function, $G(T)$, from all emission that lies outside $\log(T_{max}){\pm}0.15$. The quality factor that is used in this analysis is 0.3, meaning that up to 30% of the total contribution function for each 0.1 nm wide spectral line can come from outside the temperature range of $\log(T_{max}){\pm}0.15$. This method still allows two or more emission lines from different ions or ionization states within a given 0.1 nm range to be considered, as long as they are formed at similar temperatures. The 9.39 nm line centered on Fe XVIII in Figures 3
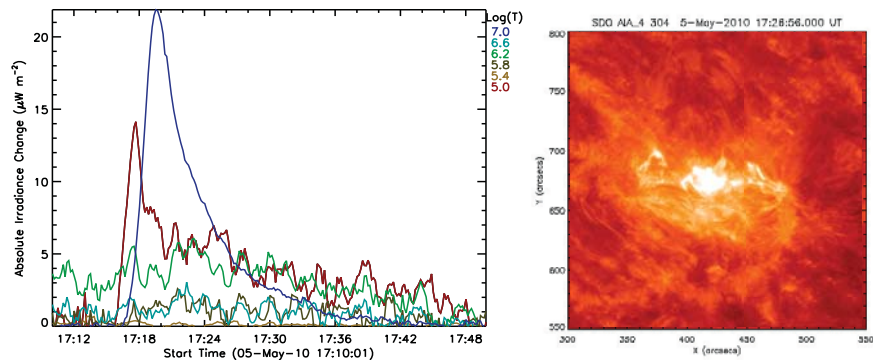

Figure 2. Temperature evolution plot and SDO/AIA 30.4 nm image for the M1.2 flare that occurred at 17 UT on 5 May 2010 at $\Delta\log(T){=}0.4$ binning.

and 4 has contributions from Fe X (formed at $\log(T)$=6.05) and Fe VIII (formed at $\log(T)$=5.75) which amount to 45% of the total contribution function. This exceeds the required 0.3 quality factor and the line is therefore not used in constructing the temperature evolution plots as it is considered blended (to within the specified 30% level). On the other hand, the 13.58 nm emission only contains 22% of emission that originates outside the desired temperature range of $\log(T)$=7.1±0.15. This emission line is therefore considered unblended and the emission line is assigned a temperature of $\log(T)$=7.1. It does have some contribution from the blends around $\log(T)$=5.6 (Ne VI; $\lesssim$7%) and $\log(T)$=5.75 (Ne VII; $\lesssim$6%), but these are considered relatively weak compared to the dominant Fe XXII emission. In constructing a thermal evolution plot, the quality factor can be set lower than 0.3, which would eliminate more blends, but at the cost of a reduction in number of emission lines used in the analysis. At a quality factor of 0.3, only about 10% of the total emission detected by EVE over the 7–37 nm range are due to 'purely' isothermal emission lines.
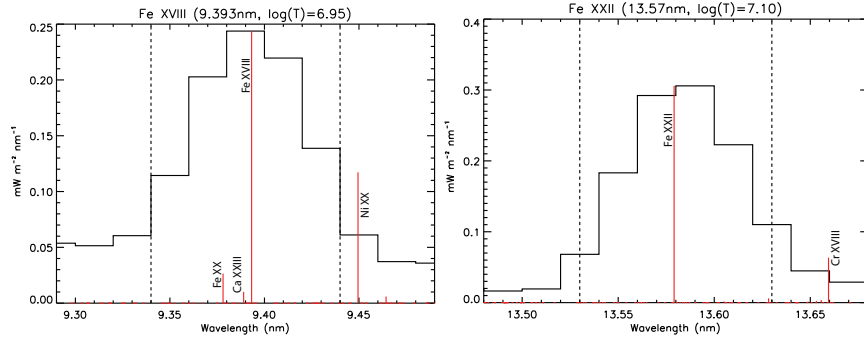

Figure 3. The two black lines are the 0.1 nm EVE resolution-limited emission lines centered on the Fe XVIII line (9.39 nm; left panel), and Fe XXII (13.58 nm; right panel). The vertical red spectra are the lines that contribute to the overall line profile as derived from CHIANTI assuming a flare DEM and an electron density of 10^{11} cm^{-3}
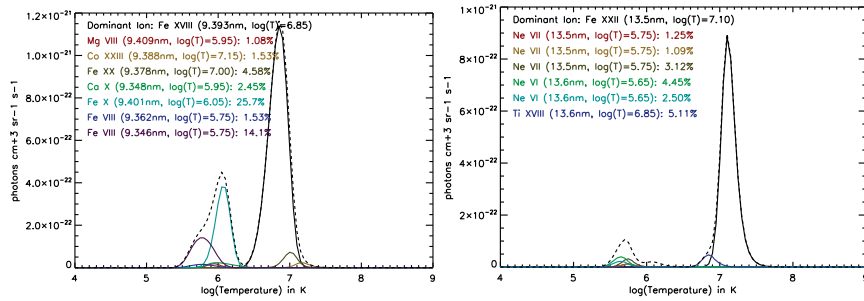

Figure 4. Contribution function from CHIANTI of the 0.1 nm range centered on 9.39 nm (left panel) and 13.58 nm (right panel). The 0.1 nm emission range on the left would be considered blended due to the significant contributions of various species over a wide temperature range, whereas the 0.1 nm range on the right would be considered unblended due to the dominance of Fe XXII emission at $\log(T)$=7.1.

An alternative method to determine if, and how much, given emissions are blended in the EVE spectra is to fully compute a high-resolution, synthetic spectrum by driving CHIANTI with various assumptions. These estimated synthetic spectra can be very different depending on the assumed flare Differential Emission Measure (DEM) and electron density that are used as inputs, but there is not a single DEM or constant electron density that can quantify the flaring plasma for all flares or even at the different times in any single flare. Using just the contribution function, as described previously, is independent of any estimated DEM or density so eliminates any assumptions that go into deriving a DEM or any subsequent synthetic spectrum; therefore, regardless of the plasma temperature distribution and the accelerated electron density or energy spectrum, this quality factor should still be valid in isolating unblended emissions in the EVE data set at all times and for all flares.

The exceptions to the above line selection criteria to use in this analysis are those from cooler, optically thick emission lines that are not correctly described in the CHIANTI database. Seven optically thick emissions are added to complete the low temperature time series in the thermal evolution plots, including transitions of the He II, C IV, and O IV ions within the MEGS-A channel and are listed in Table 1.

Table 1. Optically thick emissions added to the optically thin, unblended emission line list.

Ion	$\log(T)$	Wavelength (nm)
He II	4.9	23.733
He II	4.9	24.303
He II	4.9	25.631
He II	4.9	30.378
C IV	5.1	29.695
O IV	5.2	21.415
O IV	5.2	23.857

Along with the quality factor used to determine isothermal emission lines, the irradiance within a given 0.1 nm wavelength range must also have changed by at least $\pm 10\%$ during the X2.2 flare that occurred on 15 February 2011 to be included in the thermal evolution plot. The 'minus' is included to make sure the coronal dimmings (Woods *et al.*, 2011) are accurately represented as well and that the decreased radiated output is accurately quantified. The emission lines eliminated by this $\pm 10\%$ criteria do have a dominant, unblended emission based on the quality factor criteria, but the increased flare emissions do not increase significantly above the measurement uncertainties of EVE and would only enhance the noise and non-flaring irradiance changes. These $\pm 10\%$ variations are either coming from the instrument variations (noise or dark sensitivity) of the

emissions that is on the order of the EVE uncertainty values, or from other solar variations that are present in the irradiance measurement that dominate over the enhanced flare emissions. The combination of QF=0.3 and the X2.2 flare ±10% threshold criteria resulted in 149 individual, isothermal emission lines (including the cooler, optically thick lines) within the 6.5-37 nm range which could be used to construct the final thermal evolution plot.

Table 2. Default temperature bins for the thermal evolution plots. All temperatures are in $\log(T)$.

Bin label temp	Min temp	Max temp	Number of emissions in bin	1-sigma std. dev. μW m^{-2}	Region
5.0	4.85	5.25	6	1.53	Upper chromosphere
5.4	5.25	5.65	7	0.11	Lower trans. region
5.8	5.65	6.05	26	0.51	Upper trans. region
6.2	6.05	6.45	65	2.33	Cool corona
6.6	6.45	6.85	26	0.50	Hot corona
7.0	6.85	7.25	19	0.15	Flare corona

An example of a thermal evolution plot for the M1.2 flare which occurred on 5 May 2010 is shown in Figure 2. Time series are plotted in units of μW m^{-2} by binning together the selected unblended emission lines with appropriate values of T_{max}, and these temperature ranges and labels are listed in Table 2. An 8-minute averaged pre-flare spectra was subtracted out beforehand, eliminating most of the solar background emission from the irradiance measurements, so the resulting profiles show the timing and the absolute radiated energy over each chosen temperature range solely due to the flare. A 30-second boxcar smoothing centered on each of the native 10 second EVE integrations to was also applied to reduce the measurement noise.

The EUV spectrum is dominated by the bound-bound emission lines, but it also has underlying continua throughout this spectral range that also increase and peak at different times during flares (see Milligan *et al.* (2012)). In order to eliminate the flare-enhanced continua contributions from those of the bound-bound emissions, which may affect the timing and output of the emissions of the given temperature bins, these background continue were subtracted off from each of the emission lines. This continua contributions were quantified by first finding the minimum values on both the blue and red side of each emission line, and then fitting a line between these two points to find the value of the underlying continua in each spectral bin to be subtracted. This is done for each emission line at each time, and leaves only the enhancements for the emission line itself.

The impulsive phase enhancements in the cool, chromospheric emissions of $\log(T)$=5.0 (red curve) are seen to peak first ($\approx$ 17:18 UT). This most likely is due to the chromosphere responding to the nonthermal electrons accelerated during the flare's impulsive phase. There were also simultaneous impulsive phase enhancements up to $\log(T)$=6.2 as well indicating that the chromosphere was heated to these temperatures. The hottest emission, $\log(T)$=7.0, peaks next

around 17:20 UT, which is believed to be a result of chromospheric evaporation as chromospheric material expands upwards into the overlying loops as a result of heating due to the nonthermal electrons. This high-temperature profile closely resembles the associated GOES SXR time series which dominated by emission lines with comparable formation temperatures. The intermediate temperature profiles, $\log(T)$=6.6, 6.2, and 5.8, peak sequentially later as the flare plasma successively cools through cooler temperatures. This cooling will be discussed further in Section 3.

The $\Delta\log(T)$=0.4 does provide a moderately large temperature range, leading to a situation where the effective temperature for each bin given can be at the extreme ends rather than the mean temperature given for each of the given bins. The effective temperature may also change throughout the flare, where the effective temperature during the peak of the gradual phase will probably be at the high end of the given temperature range rather than the mean value, and towards the end of the flare may be more towards the cool end of the range. For further analyses that require a more accurate effective temperatures, the $\Delta\log(T)$ should be reduced to a small as 0.1 as seen in Figure 5.

The 1σ uncertainty on the emission in each temperature range, which is given in Table 2, was computed from a 12-hour-long, non-flaring time when a large active region was present. These uncertainty ranges include the normal measurement deviations for an EVE time series of the given bins with the 30-second boxcar smoothing, but also quantifies the solar variations in the quite Sun and active region to give and idea of the magnitude of normal, non-flaring activity that is often present in the EVE irradiance measurements; therefore, any deviations above these 1σ magnitudes over short times scales can be confidently attributed to the flare. This standard deviation was also calculated with the 8-minute mean spectrum subtracted off to make an absolute error that can be directly applied to the thermal evolution plots and energy calculations.

Although six bins with a constant $\Delta\log(T)$=0.4 were chosen for the example shown in Figure 2, and is the standard binning used throughout Section 2, the time series can be plotted over a range of temperature bins ($\Delta\log(T)$=0.1, 0.2, 0.3, 0.4, 0.6, 0.8, 1.2, and 2.4). Figure 5 shows a selection of options for viewing the thermal evolution plots in the case of the 5 May 2010 flare. Figure 5a shows the total emission integrated over the entire MEGS-A wavelength range while Figure 5b only shows the total emission integrated over all unblended lines (using QF=0.3) within this range. The overall behavior of these two profiles is remarkably similar, although the summed unblended emission profile is a factor of 10 weaker than the total emission. The unblended sum profile also has much less noise due to the restriction of emissions to those with at least a $\pm10\%$ change in irradiance described earlier, eliminating lines that only contribute noise or non-flaring irradiance emission to the profile. Figure 5c shows the flare's evolution using only the Fe lines, binned by $\log(T)$=0.1. These profiles are dominated by the hottest flare plasma at $\log(T)$>7.0. Emission at cooler temperatures do not increase much above their pre-flare levels until later in the flare as the plasma cools. There is also a lack of strong Fe emission lines below $\log(T)$=6.0 in the MEGS-A spectral range which is evident in the cooler time profiles. By adding in emission lines from other elements (Figure 5d; also at $\Delta\log(T)$=0.1), the

impulsive phase emission becomes more apparent (red curve). This emission in the $\log(T)$=5.0 bin is primarily due to the He II 30.38 nm line, the strongest line in the MEGS-A spectra, and a major radiator of flare energy in response to collisions with nonthermal electrons (Allred *et. al* 2005). This curve is comparable in strength to the $\log(T)$=7.1 curve, but as can be seen in Table 2 it is comprised of only 6 emission lines compared to the 19 lines that make up the blue curve. Using coarser temperature binning ($\Delta\log(T)$=0.2; Figure 5e) starts to reveal higher temperature ($5.9 \leq \log(T) \leq 6.3$) emission that appears synchronized with the He II emission, implying that the chromosphere is being heated to much higher temperatures by the nonthermal electrons. Finally, Figure 5f shows the flare evolution at $\Delta\log(T)$=0.4 temperature binning. The impulsive phase is still evident over a broad range of temperatures, but the hot flare emission dominates the lightcurves due to the addition of the multitude of high-temperature lines, particularly from the 8–16 nm range.

The code used to generate these plots (EVE_FLARE_TEMP_EVOL.PRO), along with its supporting routines and save-sets, will be made available to the solar physics community through SolarSoft's (Freeland and Bentley, 2000) 'EVE' branch to allows both the thermal evolution to be plotted and the EUV energy radiated to be calculated for any given flare. This code also includes a subroutine (GET_EVE_DATA.PRO) that will automatically download the most up to date EVE
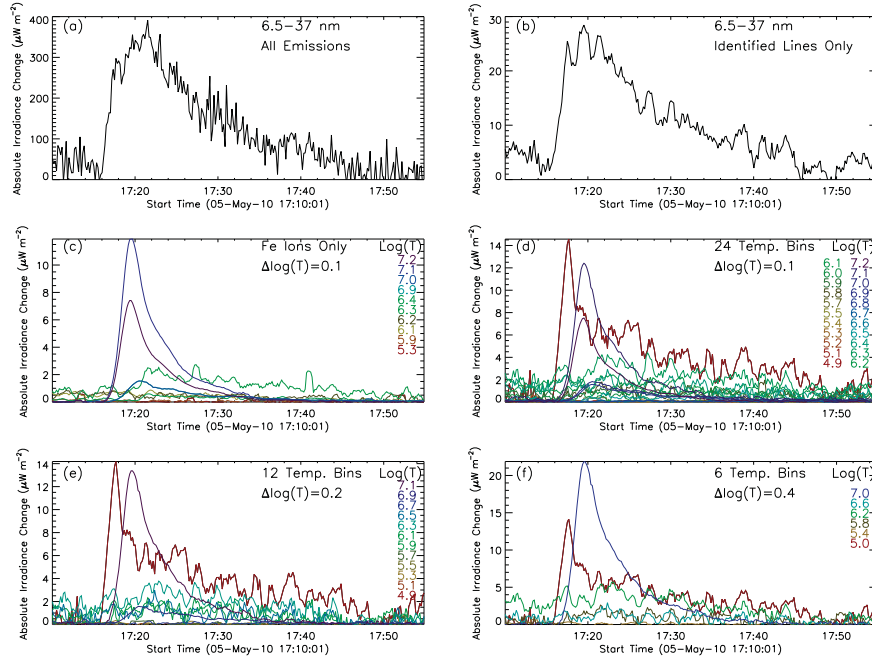

Figure 5. (a) The time series of the total flare emissions in the 6.5-37 nm wavelength range. (b) The same as (a) but just the selected, unblended emissions within this wavelength range. (c) The same as (b) but using only unblended ionization states of Fe. (d)-(f) The same as (b) but with different options of size and number of temperature bins of the unblended emissions.

data. There are also many keywords that will allow customization of the output, such as the various temperature binning schemes described above which can be tailored to the users' individual scientific goals, the specific emission lines that comprise each bin (such as only the Fe lines, or including those observed by MEGS-B, if MEGS-B was observing), plotting options such as normalizing the time series, plotting on logarithmic scales, and changing the boxcar smoothing time range. The peak time of each isothermal time series can also be plotted as a diamond symbol which allows the user to visualize the dominant temperature at a given time, which is discussed in detail in Section 3, to quantify the flare's cooling time scales, and is demonstrated.

Another key feature is the ability to manually adjust the start and stop times, or use the NOAA/GOES start and end times from the flare catalog. All plots and calculated energies given throughout this paper have been manually adjusted to completely cover the duration of the flare in all emission lines, while if the given start and end times from the GOES flare catalog are used the actual EUV radiated energy of the flare can be severely underestimated as will be discussed in Section 4 (see also Ryan *et al.* (2012)). The start time, as well as the time of the end of the impulsive phase and beginning of the gradual phase, is determined by a gaussian fit to the thermal bin containing the He II, 30.38 nm emission line and is discussed later in Section 4. The end time was determined when the hottest bin and the bin containing the He II 30.38 nm emission, which are the $\log(T)$=7.0 and $\log(T)$=5.0 bins, respectively, when using the $\Delta\log(T)$=0.4 binning, both reach values that are less than 2 μW m^{-2}. The exception to this end-time rule for the is if another flare occurs before the flare-enhanced emissions can reach below this value, which is the case for the 5 November 2010 flare that will be discussed in Section 2.3. Any radiative outputs calculated and presented for this flare should then be considered a lower bound.

The thermal evolution plots for three other flares of similar GOES magnitude to the 5 May 2010 event will now be described to show how the resulting temperature profiles differ according to their individual characteristics, such as duration, topology, complexity, and possible heating mechanisms.

2.1. M2.0 Flare - 12 June 2010

Figure 6 shows that the M2.0 flare that occurred on 12 June 2010, which showed the same 'Neupertic' behavior displayed by the 5 May 2010 flare (Section 2) with impulsive chromospheric emission peaking on the rise of the hot (>10 MK) time series. One notable difference is the temperature reached during this impulsive phase. Whereas the 5 May 2010 flare showed that the chromosphere was heated to around $\log(T)$=6.2, this event revealed temperatures of $\log(T)$=6.6 at the time of the chromospheric enhancement. It is interesting to note that the 12 June 2010 was the first gamma-ray flare of solar cycle 24 as determined from RHESSI observations (although RHESSI was off-pointing at the Crab Nebula during this event) which opens the possibility of ion beam heating in conjunction with the familiar electron beam. These new EVE observations of impulsive phase emissions seen at such high temperatures will help constrain the temperature the plasma can immediately be heated to up to during the impulsive phase of the

flare, as well as the timing that can help derive the heating rate and energy deposition in the footpoints of the flare.

The hottest flare plasma peaks 5 min later in this flare, followed by a cooling of the plasma with no further energy being injected into the system. The flare exhibits a gradual cooling over the next 5-10 min. This cooling plasma can be seen all the way down to the coolest emissions in the chromospheric bin at $\log(T)$=5.0. This impulsive flare represents the classic Neupert Effect where the impulsive phase, seen in chromospheric and transition region emissions in the red $\log(T)$=5.0 bin, precedes and is roughly the time derivative of the gradual, hot thermal phase of the flare seen as the purple $\log(T)$=7.1 bin (Neupert, 1968).

The SDO/AIA 30.4 nm image is also presented in Figure 6 to show that the spatial extent of the flare's footpoints along the ribbons is approximately 40", or about $3x10^4$ km. Note that the AIA images for the 12 June 2010 flare are saturated, as this flare occurred before the instrument's active exposure control (AEC) became operational.

2.2. M1.0 Flare - 7 August 2010

The M1.0 flare that occurred on 7 August 2010 was a two-ribbon flare, as can be seen in the He II 30.4 nm image in the right-hand panel of Figure 7 taken at 18:19 UT; the time of peak emission during the impulsive phase. Two-ribbon flares are believed to be a result of multiple reconnections, separated in time, along an arcade spanning the polarity neutral line separating the oppositely charged poles. The EVE thermal evolution plot for this flare is shown in the left-hand panel of Figure 7.

The temperature evolution plot shows that there is energy deposited into the chromosphere causing increases in cooler emissions that peak at the same time as the hottest ($\log(T)$=7.0) emission. The impulsive phase enhancements seen in the chromospheric emissions have a much more gradual increase than those seen in the previous examples. This is likely due to a continuous energy release, albeit at a lower rate, along the arcade leading to a more gradual manifestation of the
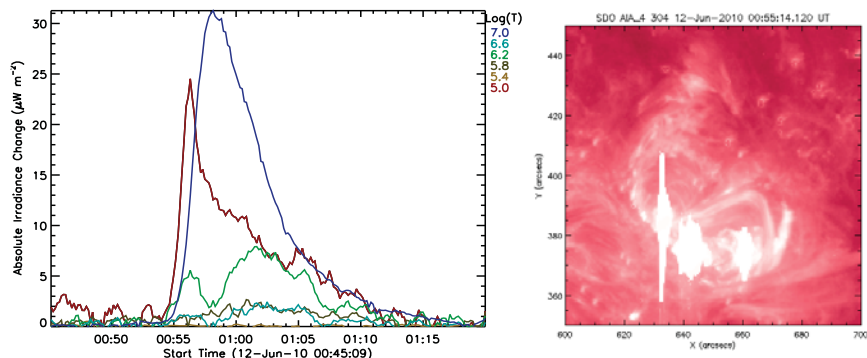

Figure 6. Flare thermal evolution as observed by EVE for the 12 June 2010 M2.0 flare (left panel) and the He II 30.4 nm image from AIA (right panel) during the impulsive phase showing the spatial extent of the chromospheric ribbons.

impulsive phase enhancements, although the peak radiation output still reaches a similar GOES magnitude as the and 12 June 2010 flares and is significantly larger than the 5 May 2010 flare.

With a more continuous energy input and longer rise phase along the flaring arcade, there is also a much longer thermal phase, with the flare peaking in the $\log(T)=7.2$ emission at 18:23 UT, about 15 minutes after the flare onset. It then takes about 20 minutes for the plasma to cool to approximately 6 MK. Therefore, the total amount of energy radiated from this flare should be significantly more than either of the previous examples due to its longer duration, regardless of the fact they are approximately the same GOES class (see Section 4).

It is also interesting to note that during this event, lightcurves of temperatures ranging from $\log(T)=5.4$ to $\log(T)=6.6$ all peak around the same time (18:43 UT). It is unclear from the plots alone whether this is a signature of heating or cooling, or a balance between the two.

2.3. M1.0 Flare - 5 November 2010

The radiative output at various temperatures for the M1.0 class solar flares on 5 November 2010 is shown in Figure 8. The end time of this flare is close, but does meet the end-time criteria discussed previously due to another flare that starts at approximately 15:30 UT. Some of the cooler, enhanced emissions from this later flare may be seen starting towards the end of this flare.

The 5 Nov 2010 flare is a much more gradual flare than either the 5 May 2010 or 12 June 2010 ones, with a rise time of 15-20 minutes; similar to the 7 August 2010 flare. What is notably absent from the thermal evolution plot shown in Figure 8, however, is the distinct lack of impulsive phase emission at chromospheric temperatures that usually precedes the hottest emission. The thermal evolution plots for this flare do show an increase in the $\log(T)=4.9$ emissions during the thermal phase near the peak of the $\log(T)=7.1$ emissions however, although without any enhanced emission during the impulsive phase
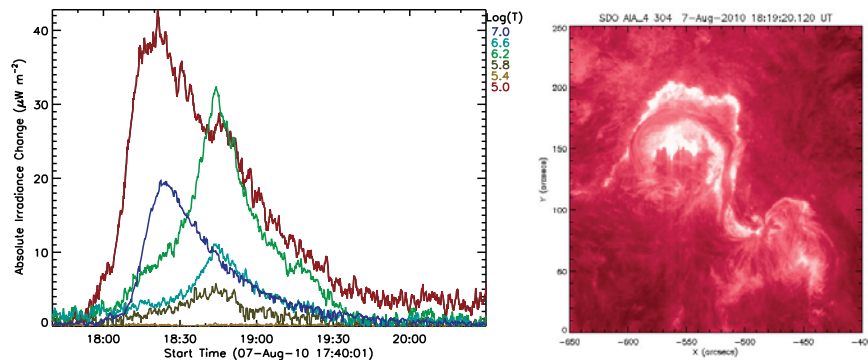

Figure 7. Flare temperature evolution for a two-ribbon flare observed by EVE for the 7 Aug 2010 M1.0 flare (left hand panel) and the corresponding AIA 30.4 nm image showing the two ribbon footpoints (right hand panel).

implies that there was not a significant enough density of accelerated particles impacting the chromosphere and transition region[1]. The slight increase in chromospheric emission that was observed may have therefore been a result of thermal conduction fronts emanating in the corona, or perhaps photoionization of the He II 30.38 nm line by SXR photons.
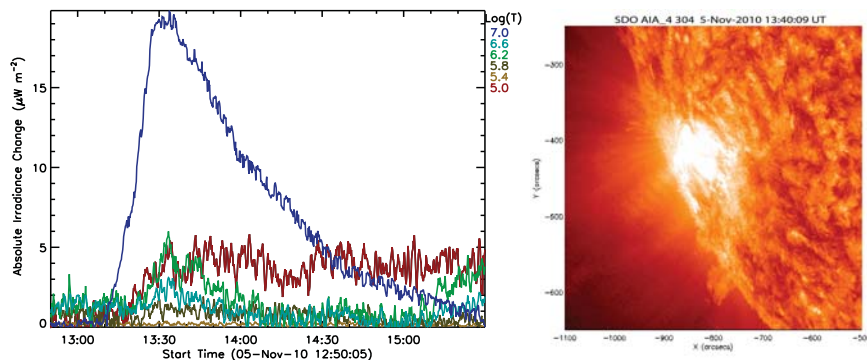

Figure 8. Flare thermal evolution as observed by EVE for the 5 November 2010 M1.0 flare that lacked clearly defined impulsive phase emission in the $\log(T)=5.0$ temperature bin (red line; left hand panel). Right panel: An AIA 30.4 nm image of the flare taken near the peak of the flare.

It is important to discuss here whether this flare lacked any observed impulsive phase emission due to its location on the visible disk, as optically thick emissions have been shown to decrease at large heliographic angles - the center-to-limb-variation. This effect has been previously observed in both active regions (Worden, Woods, and Bowman, 2001) as well as in flares (Chamberlin, Woods, and Eparvier, 2008). The 16 October 2010 flare occurred 76° away from the disk center, while the 5 November 2010 flare was 73° away. The reduced impulsive phase emission of optically thick lines due to absorption and scatter should have been similar in both events. Even with the center-to-limb absorption expected to fall off as a cosine function toward the limb there should still have been a significant enhancement of impulsive phase emissions for the 5 November 2010 flare if it really existed. This supports the conclusion that the 5 November 2010 flare truly lacked an impulsive phase.

3. Flare Cooling Rate

The cooling rate of the flaring plasma can be determined by using the time of peak emission for each temperature bin in the thermal evolution plots. The peak time can be determined by overplotting diamond symbols at the time of

---

[1]It has been confirmed that the 5 November 2010 flare also had no detectable hard X-ray emission from spectroscopic analysis of RHESSI observations, but an in depth discussion between EVE and RHESSI data for the events presented here is being prepared in a separate paper.

the peak emission for each temperature and fitting them with a linear function. An example for the 12 June 2010 flare can be seen in Figure 9. For this flare, the peak temperature 'diamonds' for the $\log(T)$=6.8 and $\log(T)$=6.6 bins were eliminated as there was not significant flare increase for these bins above the 1σ noise values given in Table 2. The cooling rate is determined by the slope of a linear fit of these peak emission temperatures as a function of time for temperature bins greater than $\log(T)$=5.3, and can be seen in the third column of Table 3 for all the flares presented previously. The 1σ uncertainties of the linear fit for the cooling rate are also listed, demonstrating that the uncertainties of this fit are usually 10-20%.
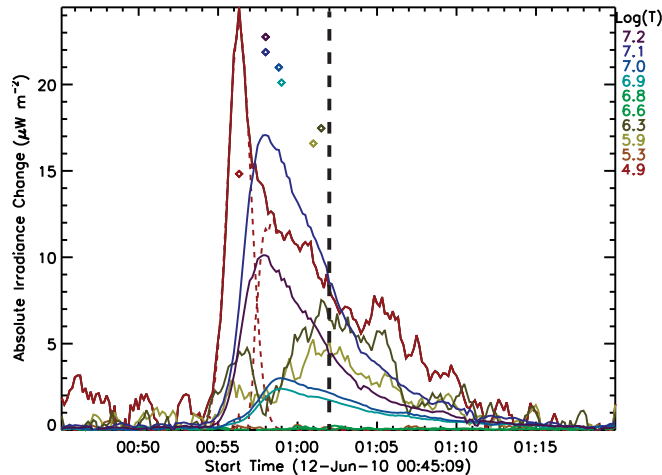

Figure 9. Temperature evolution plot with peak emission times for each thermal bin for the flare that occurred on 12 June 2010. The thermal binning for this plot have $\Delta\log(T)$=0.1 bins for $T \geq 6.8$, with gradually larger bins for the cooler emissions. The diamonds show the time of the peak emission for each temperature bin, showing the cooling of the flare plasma. The left-most dashed red line signifies the impulsive phase, the determination of which is discussed in Section 4, and the right-most dashed line is the residual representing the gradual phase emission in this temperature bin. The vertical dashed black lines show the NOAA end-time of the flare, demonstrating how much additional radiated energy occurs after this stated end time.

There are a range of temperatures observed in all flares during their decay phases, but the diamonds symbolize the temperature of the bulk of the plasma at a given time. Determining the cooling rate by this method is valid in impulsive flares after the peak of the gradual phase when the energy release, and therefore the heating, has stopped. However, this may not be valid for the two-ribbon flares as there is still continued energy release and heating, just at a smaller rate, even after the peak of the gradual phase (Warren, 2006), and is a highly multi-thermal plasma during most of the flare.

The thermal evolution plots and data provided by the wide range of isolated emissions of a given formation temperature will help to constrain theories of the plasma cooling during a solar flare. Future analysis of flare-heated plasma as it cools can be compared with models of radiative and conductive cooling, such as

those of Cartill *et al.* (1995) or Klimchuk *et al.* (2008), as well as extending the impulsively heated nanoflare cooling model of Bradshaw and Klimchuk (2011) to larger flares. These analyses will be important to determine the different cooling rates at different times during the gradual phase based on when the radiative or conductive cooling dominates, whereas the cooling rates given in Table 3 are a simplified linear fit through the entire cooling regardless of the dominant cooling mechanism.

4. Flare Radiative Output from 0.1-37 nm

Section 2 described four flares with notably different thermal evolutions. This section aims to compare the absolute energy radiated for each flare, which are summarized in Table 4. Listed are the absolute radiated energies for the flares during both the impulsive and gradual phases as well as for various wavelength bins. In order to determine the total energy output in ergs for the EVE/MEGS spectral data, the W m^{-2} nm^{-1} irradiance time series (after pre-flare irradiance values were subtracted) is integrated over time and the given wavelength range to get J m^{-2}. This is then multiplied by 2.812x10^{29} to convert to ergs given MEGS' 0.02 nm spectral bins. The conversion factor for the ESP diodes, due to the fact it is broadband from 0.1-7nm, is given in units of W m^{-2}, and is also at 10 second integrations (at Level 2 data product), gives an ESP-specific conversion factor of 1.406x10^{31}. It should also be noted that this integration over wavelength bins is independent of the radiative source mechanism, and can include contributions from free-free and free-bound continua as well as from the bound-bound emissions describe above. Comparisons of the radiative output between these three emission during a flare using MEGS data is discussed in detail in Milligan *et al.* (2012).

The radiated energies for an additional flare was added to the table that have a smaller peak GOES magnitude, the C3.2 long-duration flare on 1 August 2010 that had 10+ MK thermal plasma that lasted for over two hours. This flare was used to make another comparison using a different variable, the peak GOES soft X-ray magnitude that is almost an order of magnitude lower but shows much larger radiated values compared to the M-class flares.

Table 3. Flare cooling rates derived from fits to the time of peak emission from the temperature bins in the flare evolution plots.

Date	GOES class	Cooling rate K/sec (10^4)	Cooling rate fit uncertainty (%)	0.1-37.0 nm energy (10^{28})	Temp (MK)
5-May-10	M1.2	6.5	16	193	16
12-Jun-10	M2.0	6.9	8	257	21
7-Aug-10	M1.0	0.87	12	1684	13
5-Nov-10	M1.0	1.75	14	1364	14
1-Aug-10	C3.2	0.28	10	1484	11

To quantify the radiated output for both the impulsive phase and gradual phase separately, the timing of each of these phases needs to first be determined. The timing of the impulsive phase was determined by fitting a gaussian to the temperature bin that is dominated by the He ɪɪ 30.38 nm emission line, but with the condition that the peak time must occur prior to the peak in the hottest temperature bin. This condition helps to correctly attribute the gradual phase emissions in flares lacking impulsive phase emissions, such as the 5 November 2010 flare. The Guassian fit was only performed on the rise of the time series so as not to include the gradual phase emissions that have increased during the decay time of the impulsive phase or due to the know Si xɪ blend that is within the spectral resolution of the He ɪɪ peak and can contribute to a perceived and prolonged gradual phase. The timing of the impulsive phase is defined as the 2-sigma width of this Gaussian fit to the thermal bin with the He ɪɪ emission, where the flare start time is also defined as the start of the impulsive phase. The impulsive phase emissions are then those that occur within this 2-sigma width while the gradual phase emissions are the emissions that occur after the end of the impulsive phase until the end of the gradual phase, which is either defined manually as described in Section 2 or automatically using the NOAA flare end time.

This gaussian fit can be seen in Figure 9 as the left-most dashed red line signifying the impulsive phase, where the right-most dashed line is the residual representing the gradual phase emission in this temperature bin. The start and end times for this flare was determined manually by looking at the flare light curves. The energies can also be derived using the GOES start and end times. These were used to obtain the radiated energies in parenthesis in Table 4. As can be seen in Table 4 these the GOES flare times are very restrictive, especially for the gradual phase when many of the dominant and bright cooler emissions are still radiating above the pre-flare background level. In some cases, the gradual phase energy was underestimated by more then 300% when using the GOES times. The GOES end time for the 12 June 2010 flare (01:02 UT) is plotted as a vertical black dashed line in Figure 9, showing the early NOAA end-time that

Table 4. Flare radiative energy release in various wavelength bins and flare phases. The energy values in parenthesis were calculated using the GOES start and end times for the flare that do not account for the entire range of the flare.

Date	GOES class	Helio angle (deg)	GOES 0.1-0.8 nm energy	ESP 0.1-7.0 nm energy	MEGS-A 7-37 nm imp. ph.	MEGS-A 7-37 nm grad. ph.	Max. temp (MK)
			All energies are given in 10^{28} ergs				
5-May-10	M1.2	56	1.2	127 (53)	5 (4)	63 (10)	16
12-Jun-10	M2.0	25	1.9	199 (126)	6 (6)	47 (21)	21
7-Aug-10	M1.0	35	5.7	1097 (622)	135 (100)	420 (107)	13
5-Nov-10	M1.0	73	7.4	1119 (612)	( )	270 (106)	14
1-Aug-10	C3.2	35	5.4	1055 (445)	77 (66)	379 (84)	11

would cut off significant radiation and cause the energies to be underestimated in Table 4.

Along with breaking down the radiated energy into impulsive and gradual phases in Table 4, it is also shown in three separate instrument/channel-defined wavelength bands. The shortest wavelength, soft X-ray band is the 0.1-0.7 nm band that is measured by the GOES XRS B-channel. Another, broader soft X-ray band ranging from 0.1-7.0 nm is measured by the ESP channel on EVE. The third wavelength range shown in Table 4 is the range from 7.0-37.0 nm from the MEGS-A channels. This was truncated from the complete MEGS-A wavelength range that extends down to 6.5 nm so as not to overlap the energy bin from the ESP channel. This band has significant contributions from both the impulsive and gradual phase due to the large temperature range of its emissions, so it is broken down into the contributions from each flare phase. The maximum temperature is also shown, which is derived from a ratio of the two GOES XRS channels (Garcia, 2000; White, Thomas, and Schwartz, 2005).
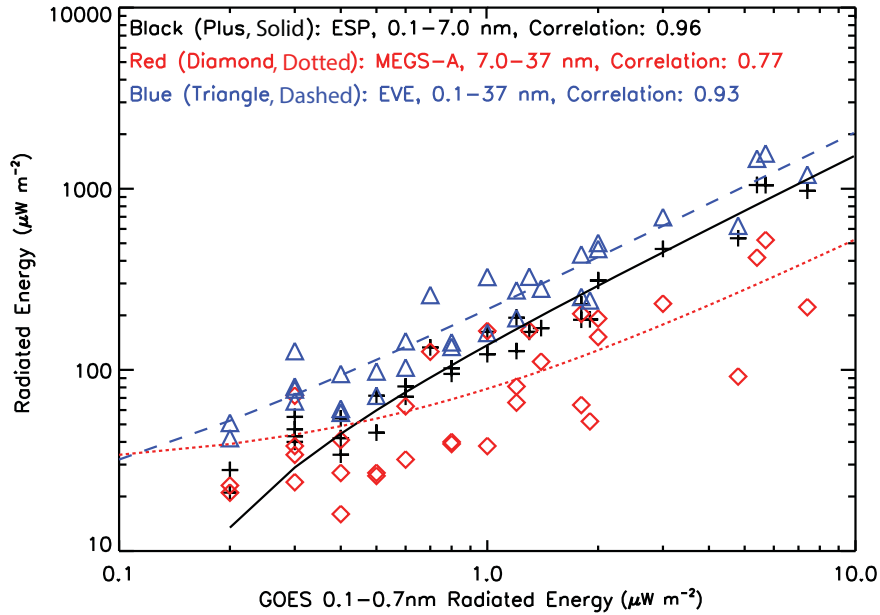

Figure 10. Linear fits and correlation of the radiated energy of the GOES XRS band to three different EVE wavelength bands, showing good correlation between the thermally dominated soft X-ray emissions (blue triangles) but a much weaker correlation to the EUV emissions that have a significant contribution from non-thermal emissions (red diamonds).

The total radiated output from the various wavelength bands are linearly correlated, where the plot, fit, and correlations of the 0.1-0.8 nm from GOES XRS to the three wavelength bands of 0.1-7.0 nm from EVE ESP, 7-37 nm from EVE MEGS, and the total EVE 0.1-37 nm band can be seen in Figure 10. This figure includes the measured radiated output for 32 flares, which are all the flares of C2.0 and above that occurred from 1 May 2010 to 31 December 2010

but excludes over-the-limb flares with occulted footpoints that could erroneously cause the impulsive phase output to be low. This figure shows a strong correlation (0.96) between the soft X-ray emissions of GOES XRS and EVE ESP that are dominated by thermal emissions (blue triangles). The correlation (0.77) is much weaker between the soft X-ray emissions from GOES soft X-ray and the EUV emissions from EVE MEGS, seen by the red diamonds, as the MEGS emissions have a significant contribution (8-30%, derived from Table 4 from the impulsive phase enhancements of its cooler emissions. The correlation (0.93) between the 0.1-0.7 nm and the entire 0.1-37 nm broad wavelength range is again strong, as the 0.1-37 nm flare enhancements are dominated by the short wavelength (0.1-7.0 nm) thermal components that can be up to a factor of five of this larger wavelength band (again derived from Table 4).

There can be a large range of total radiated energy in both the impulsive and gradual phases for any magnitude GOES class flare. This can easily be seen in comparing the radiated emissions in the additional low C-class flare in Table 4 to the previously presented low M-class flares. It can be seen that the C3.2 flare on 1 Aug 2010 has much more radiated energy than almost all of the M-class flares except the 7 Aug 2010 flare, where the total radiated energy is almost comparable.

5. Discussion

The ability to measure the temperature evolution of flaring plasma at high cadence, and with high photometric precision, marks an important use of EVE data for determining the heating and cooling processes responsible. The 'standard' flare model (CHSKP; Kopp and Pneuman, 1976) states that following an episode of magnetic reconnection in the corona, high energy electrons are accelerated along newly connected magnetic field lines until they collide with the dense, underlying chromosphere producing heating and HXR emission. The heated material subsequently expands, filling the overlying coronal loop system which is visible at >10 MK temperatures. The flares discussed in Section 2 show that high temperature plasma can exist during flares of similar magnitude, whether or not a chromospheric counterpart is evident. This would suggest that the chromospheric evaporation scenario is not the complete story (or only occurs is certain circumstances) and other heating mechanisms may need to be considered, such as direct (shock) heating at the reconnection site in the corona.

Flares, such as the 5 November 2010 flare, show that there can be flares with no impulsive phase emission in the EUV, similar to the SMM observations by Dennis (1985) and also in the through analysis of the GOES XRS data (McTiernan, Fisher, and Li, 1999). This demonstrates that the direct heating from the energy release at the reconnection site can be an efficient process that either inhibits particle acceleration from either happening to begin with or causes the accelerated particles to be stopped and deposit their energy while still in the coronal loop before reaching the cooler chromosphere and lower transition region, being a completely thermal flare. This was also theorized by Tanaka (1983) that a contributing factor for different flare types may be the coronal density prior to

the flare initiation. With the complete and continuous observations from EVE providing better statistics, flares having no impulsive phase emissions has been confirmed and can no longer be completely explained by the absorption and scattering of increased footpoint emissions in the optically thick emissions near the limb of the solar disk as it has been previously (Chamberlin, Woods, and Eparvier, 2008; Woods, Kopp, and Chamberlin, 2006).

In the impulsive flare plots of 5 May 2010 and 12 June 2010, Figures 2, 6 and 9, the timing of the gradual phase peak emissions in the various temperature bins is clearly observed to occur at different times. In these flares, the peak emissions show a distinct cooling, with the hotter emissions peaking before the cooler and would have a narrower temperature distributions, although it can clearly be seen that there are flare emissions at all temperatures. Flares, such as the 16 October 2010 flare, can show a much larger, multi-thermal temperature range, and show a more coordinated emission time series that all peak at approximately the same time (within a minute). EVE will be beneficial in redefining the plasma flare distribution at times during flares due to its temporal and spectral resolution, refining flare DEMs. Also shown with the various examples is that there is probably not a single 'standard' flare DEM, as different flares will have a different distribution of plasma at various temperatures and at different times throughout the flare evolution.

The flares discussed here have a range of temperatures that shown an impulsive phase enhancement. For some flares, such as the 5 May 2010 M1.2 event, there is a distinct impulsive phase enhancement to temperatures up to $\log(T)$=6.3, while in the 16 June 2010 flare the impulsive phase emissions can be seen up to $\log(T)$=6.8. This signifies the maximum temperature that the locally heated plasma reaches in the chromosphere during chromospheric evaporation prior to chromospheric evaporation. Blue-shifted emissions with temperatures of $\log(T)$=6.8 have been previously observed during flares, which is evidence of the upward flowing chromospheric expansion, using the high spectral resolution and spatial imaging from *HINODE* EIS (Hara *et al.*, 2011).

How the thermal evolution profiles at the various temperatures relates to the heating rate and explosive chromospheric evaporation needs further examination. This can be done with comparisons of the $\log(T)$=4.9 emission profiles of the optically thick, chromospheric and transition region emissions with RHESSI hard X-ray emissions and the derived accelerated electron beam profiles that can be inferred from these measurements. Also, by combining EVE and RHESSI data with theoretical models such as the ones by (Allred *et al.*, 2005) further progress in understanding the dynamics of plasma transport during the impulsive phase of flares can be achieved. A future study will involve looking at the timing of these impulsive phase peaks for the large range of impulsive temperature emissions, while once again comparing to the RHESSI hard X-ray profiles, to look at the timings of the flare footpoint energy deposition and heating.

The radiative output during flares has been shown to be accurately quantified at all wavelengths throughout the soft X-rays and EUV, which is one of the primary goals of the EVE mission. These EVE measurements are already being utilized in studies of flare effects on Earth's ionosphere and thermosphere demonstrating the impact the measurements have on aeronomy studies, validating SDO's role in NASA's Living With a Star Program.

6. Conclusions

This study has demonstrated that SDO EVE accurately measures the EUV radiated output of solar flares over a large temperature range from 80 000K to 20+ MK. These measurements are a critical component in determining the total flare and solar eruptive event energy budget as well as investigating solar flare heating and the subsequent cooling mechanisms. EVE observations, along with multiple other resources and observations from the Great Heliophysics Observatory, are necessary to continually refine the standard flare model. Other complimentary instruments for further detailed studies to provide this larger picture include the RHESSI spacecraft to look at the source electron beam characteristics with the hard X-ray spectra, the Atmospheric and Imaging Assembly (AIA) instrument onboard SDO that can give EUV images at high temporal resolution and multiple temperatures. Also of interest are flare observations from scanning slit imaging spectrometers, such as SOHO SUMER and CDS as well as *HINODE EIS*. Using fits to the hard X-ray nonthermal emission spectrum, along with the emitting area given by images, during a solar flare have potential to derive the electron beam density and energy spectra during solar flare. These collaborative measurements, along with the measurements from EVE, have the potential to diagnose these properties and may lead to new results of the energetics of the initial stages of a solar flare.

References

Allred, J.C., Hawley, S.L., Abbett, W.P., Carlsson, M.: 2005, Radiative hydrodynamic models of the optical and ultraviolet emission from solar flares. *Astrophys. J.* **630**, 573 – 586. doi:**10.1086/431751**.

Bradshaw, S.J., Klimchuk, J.A.: 2011, What Dominates the Coronal Emission Spectrum During the Cycle of Impulsive Heating and Cooling? *Astrophys. J. Suppl.* **194**, 26+. doi:**10.1088/0067-0049/194/2/26**.

Cargill, P.J., Mariska, J.T., Antiochos, S.K.: 1995, Cooling of solar flares plasmas. 1: Theoretical considerations. *Astrophys. J.* **439**, 1034 – 1043. doi:**10.1086/175240**.

Chamberlin, P.C., Woods, T.N., Eparvier, F.G.: 2008, Flare Irradiance Spectral Model (FISM): Flare component algorithms and results. *Space Weather* **6**, 5001. doi:**10.1029/2007SW000372**.

Dennis, B.R.: 1985, Solar hard X-ray bursts. *Solar Phys.* **100**, 465 – 490. doi:**10.1007/BF00158441**.

Dere, K.P., Landi, E., Mason, H.E., Monsignori Fossi, B.C., Young, P.R.: 1997, CHIANTI - an atomic database for emission lines. *Astron. Astrophys. Suppl.* **125**, 149 – 173. doi:**10.1051/aas:1997368**.

Dere, K.P., Landi, E., Young, P.R., Del Zanna, G., Landini, M., Mason, H.E.: 2009, CHIANTI - an atomic database for emission lines. IX. Ionization rates, recombination rates, ionization equilibria for the elements hydrogen through zinc and updated atomic data. *Astron. Astrophys.* **498**, 915 – 929. doi:**10.1051/0004-6361/200911712**.

Didkovsky, L., Judge, D., Wieman, S., Woods, T., Jones, A.: 2009, EUV SpectroPhotometer (ESP) in Extreme ultraviolet Variability Experiment (EVE): Algorithms and calibrations. *Solar Phys.*, 182. doi:**10.1007/s11207-009-9485-8**.

Donnelly, R.F., Kane, S.R.: 1978, Impulsive extreme-ultraviolet and hard X-ray emission during solar flares. *Astrophys. J.* **222**, 1043−1053. doi:10.1086/156222.

Freeland, S., Bentley, R.: 2000, SolarSoft. In: Murdin, P. (ed.). *Encyclopedia of Astronomy and Astrophysics*, article 3390. doi:10.1888/0333750888/3390.

Garcia, H.A.: 2000, Thermal-spatial analysis of medium and large solar flares, 1976 to 1996. *Astrophys. J. Suppl.* **127**, 189−210. doi:10.1086/313312.

Hara, H., Watanabe, T., Harra, L.K., Culhane, J.L., Young, P.R.: 2011, Plasma motions and heating by magnetic reconnection in a 2007 May 19 flare. *Astrophys. J.* **741**, 107. doi:10.1088/0004-637X/741/2/107.

Hudson, H.S.: 2011, Global properties of solar flares. *Space Sci. Rev.* **158**, 5−41. doi:10.1007/s11214-010-9721-4.

Kane, S.R., Donnelly, R.F.: 1971, Impulsive hard X-ray and ultraviolet emission during solar flares. *Astrophys. J.* **164**, 151−. doi:10.1086/150826.

Klimchuk, J.A., Patsourakos, S., Cargill, P.J.: 2008, Highly efficient modeling of dynamic coronal loops. *Astrophys. J.* **682**, 1351−1362. doi:10.1086/589426.

Kopp, R.A., Pneuman, G.W.: 1976, Magnetic reconnection in the corona and the loop prominence phenomenon. *Solar Phys.* **50**, 85−98. doi:10.1007/BF00206193.

Lemen, J.R., Title, A.M., Akin, D.J., Boerner, P.F., Chou, C., Drake, J.F., Duncan, D.W., Edwards, C.G., Friedlaender, F.M., Heyman, G.F., Hurlburt, N.E., Katz, N.L., Kushner, G.D., Levay, M., Lindgren, R.W., Mathur, D.P., McFeaters, E.L., Mitchell, S., Rehse, R.A., Schrijver, C.J., Springer, L.A., Stern, R.A., Tarbell, T.D., Wuelser, J.-P., Wolfson, C.J., Yanari, C., Bookbinder, J.A., Cheimets, P.N., Caldwell, D., Deluca, E.E., Gates, R., Golub, L., Park, S., Podgorski, W.A., Bush, R.I., Scherrer, P.H., Gummin, M.A., Smith, P., Auker, G., Jerram, P., Pool, P., Soufli, R., Windt, D.L., Beardsley, S., Clapp, M., Lang, J., Waltham, N.: 2012, The Atmospheric Imaging Assembly (AIA) on the Solar Dynamics Observatory (SDO). *Solar Phys.*, 172. doi:10.1007/s11207-011-9776-8.

McTiernan, J.M., Fisher, G.H., Li, P.: 1999, The solar flare soft X-ray differential emission measure and the Neupert effect at different temperatures. *Astrophys. J.* **514**, 472−483. doi:10.1086/306924.

Mendillo, M., Withers, P., Hinson, D., Rishbeth, H., Reinisch, B.: 2006, Effects of solar flares on the ionosphere of Mars. *Science* **311**, 1135−1138. doi:10.1126/science.1122099.

Milligan, R.O., Chamberlin, P.C., Hudson, H.S., Woods, T.N., Mathioudakis, M., Fletcher, L., Kowalski, A.F., Keenan, F.P.: 2012, Observations of enhanced extreme ultraviolet continua during an X-class solar flare Using SDO/EVE. *Astrophys. J. Lett.* **748**, L14. doi:10.1088/2041-8205/748/1/L14.

Neupert, W.M.: 1968, Comparison of solar X-ray line emission with microwave emission during flares. *Astrophys. J. Lett.* **153**, L59. doi:10.1086/180220.

Pawlowski, D.J., Ridley, A.J.: 2008, Modeling the thermospheric response to solar flares. *J. Geophys. Res.* **113**, 10309. doi:10.1029/2008JA013182.

Pesnell, W.D., Thompson, B.J., Chamberlin, P.C.: 2012, The Solar Dynamics Observatory (SDO). *Solar Phys.* **275**, 3−15. doi:10.1007/s11207-011-9841-3.

Qian, L., Burns, A.G., Chamberlin, P.C., Solomon, S.C.: 2010, Flare location on the solar disk: Modeling the thermosphere and ionosphere response. *J. Geophys. Res.)* **115**, 9311. doi:10.1029/2009JA015225.

Ryan, D.F., Milligan, R.O., Gallagher, P.T., Dennis, B.R., Tolbert, A.K., Schwartz, R.A., Young, C.A.: 2012, The thermal properties of solar flares over the past three solar cycles using GOES X-ray observations. *Astrophys. J. Suppl.*, Submitted.

Sternovsky, Z., Chamberlin, P., Horanyi, M., Robertson, S., Wang, X.: 2008, Variability of the lunar photoelectron sheath and dust mobility due to solar activity. *J. Geophys. Res.* **113**, 10104. doi:10.1029/2008JA013487.

Sutton, E.K., Forbes, J.M., Nerem, R.S., Woods, T.N.: 2006, Neutral density response to the solar flares of October and November, 2003. *Geophys. Res. Lett.* **33**, 22101. doi:10.1029/2006GL027737.

Tanaka, K., Watanabe, T., Nitta, N., Akita, K.: 1983, Interpretation of the soft X-ray spectra from HINOTORI. *Solar Phys.* **86**, 91−100. doi:10.1007/BF00157177.

Warren, H.P.: 2006, Multithread hydrodynamic modeling of a solar flare. *Astrophys. J.* **637**, 522−530. doi:10.1086/497904.

White, S.M., Thomas, R.J., Schwartz, R.A.: 2005, Updated expressions for determining temperatures and emission measures from GOES soft X-ray measurements. *Solar Phys.* **227**, 231−248. doi:10.1007/s11207-005-2445-z.

Withers, P.: 2009, A review of observed variability in the dayside ionosphere of Mars. *Adv. Space Res.* **44**, 277 – 307. doi:10.1016/j.asr.2009.04.027.

Woods, T.N., Kopp, G., Chamberlin, P.C.: 2006, Contributions of the solar ultraviolet irradiance to the total solar irradiance during large flares. *J. Geophys. Res.* **111**, 10. doi:10.1029/2005JA011507.

Woods, T.N., Eparvier, F.G., Bailey, S.M., Chamberlin, P.C., Lean, J., Rottman, G.J., Solomon, S.C., Tobiska, W.K., Woodraska, D.L.: 2005, Solar EUV Experiment (SEE): Mission overview and first results. *J. Geophys. Res.)* **110**, 1312. doi:10.1029/2004JA010765.

Woods, T.N., Hock, R., Eparvier, F., Jones, A.R., Chamberlin, P.C., Klimchuk, J.A., Didkovsky, L., Judge, D., Mariska, J., Warren, H., Schrijver, C.J., Webb, D.F., Bailey, S., Tobiska, W.K.: 2011, New solar extreme-ultraviolet irradiance observations during flares. *Astrophys. J.* **739**, 59. doi:10.1088/0004-637X/739/2/59.

Woods, T.N., Eparvier, F.G., Hock, R., Jones, A.R., Woodraska, D., Judge, D., Didkovsky, L., Lean, J., Mariska, J., Warren, H., McMullin, D., Chamberlin, P., Berthiaume, G., Bailey, S., Fuller-Rowell, T., Sojka, J., Tobiska, W.K., Viereck, R.: 2012, Extreme ultraviolet Variability Experiment (EVE) on the Solar Dynamics Observatory (SDO): Overview of science objectives, instrument design, data products, and model developments. *Solar Phys.* **275**, 115 – 143. doi:10.1007/s11207-009-9487-6.

Worden, J.R., Woods, T.N., Bowman, K.W.: 2001, Far-ultraviolet intensities and center-to-limb variations of active regions and quiet Sun using UARS SOLSTICE irradiance measurements and ground-based spectroheliograms. *Astrophys. J.* **560**, 1020 – 1034. doi:10.1086/323058.